aerospace

MDPI

Article

Computational Study of Fluidic-Valve Injectors for Detonation Engines

Jayson Craig Small and Liwei Zhang *

Aerodynamics Research Center, Department of Mechanical and Aerospace Engineering, University of Texas at Arlington, Arlington, TX 76019, USA; jayson.small@mavs.uta.edu
* Correspondence: liwei.zhang@uta.edu

Abstract: The performance of detonation engines depends on propellant injectors. This study investigates a fluidic-valve injector mounted to a detonation tube. The injector is equipped with a recessed cavity connecting to the fuel plenum. After verifying the theoretical and numerical framework, three cases (I, II, and III) are analyzed, each representing different combinations of initial injector conditions and fuel supply setups. In all cases, a detonation wave is initiated near the headend of the detonation tube. It propagates through the initial section of the tube and undergoes diffraction and deformation at the flush-wall orifice. Among the considered cases, Case III, featuring a pre-pressurized initial injector flowfield and a total-pressure-inlet boundary, demonstrates the best agreement with the experimental results. It reveals a strong interaction between the longitudinally traveling detonation wave and the transverse propellant plume expanding from the orifice, causing the detonation wave to split. One part continues within the tube, while the other diffracts into the injector, creating a recirculation zone. Shock waves propagate within the injector and reflect at the base of the cavity, generating pressure spikes similar to the experimental observations. However, the contact surface separating the burnt products and fresh propellant reaches only a limited distance into the injector, suggesting a short interruption time and rapid recovery of the propellant supply.

Keywords: injector; numerical setups; detonation

check for updates

Citation: Small, J.C.; Zhang, L. Computational Study of Fluidic-Valve Injectors for Detonation Engines. *Aerospace* **2024**, *11*, 171. https://doi.org/10.3390/aerospace11030171

Academic Editor: Bo Zhang

Received: 19 January 2024
Revised: 13 February 2024
Accepted: 19 February 2024
Published: 21 February 2024

Copyright: © 2024 by the authors. Licensee MDPI, Basel, Switzerland. This article is an open access article distributed under the terms and conditions of the Creative Commons Attribution (CC BY) license (https://creativecommons.org/licenses/by/4.0/).

1. Introduction

With the potential for greater fuel efficiency, higher energy density, and lighter weight over traditional propulsion systems, detonation engines have been considered for a wide range of applications in aviation and space flight over the past few decades [1–4]. One of the leading concepts is the continuously rotating detonation engine (RDE). Many studies have been performed of various configurations, including premixed propellant injection [5], separate fuel and oxidizer injection [6], and concepts using pure oxygen or air as the oxidizer [7,8]. With each configuration comes different demands on the fueling scheme, to supply a steady and quality propellant stream to the detonation wave.

With annulus diameters between 0.1 and 1.0 m, the nominal operating frequencies of RDEs range from 1 to 10 kHz [9], which poses severe challenges for injector design. One of the primary challenges is the lack of traditional solenoid valves capable of operating at such high frequencies [10]. To address this issue, a valveless injector has been proposed to utilize gas-dynamic processes to serve the function of a valve [9,11]. The valveless injector, also known as a fluidic-valve injector, consists of an injection orifice open to a detonation tube and a recessed cavity with its base connected to the propellant feed line. When a detonation wave passes the orifice, a blast wave is diffracted into the injector, inducing high pressure in the cavity that blocks the propellant from entering the detonation tube. Peace et al. [11] mounted the injector to a pulsed detonation engine (PDE) operating at 20 Hz and analyzed the interruption time interval, defined as the time period during which detonation burnt products reside in the cavity. By adjusting the cavity length and propellant supply line pressure, they achieved controlled interrupted propellant flow.

Another challenge occurring in systems with separate fuel and oxidizer supplies is the mixing phenomenon. The high frequency of the detonation wave traveling around the annular chamber limits the interactions between fuel and oxidizer, resulting in propellants that are insufficiently mixed. Additionally, the transient mixing process between unburned propellants and burnt products reduces the detonation wave speed [12] and, consequently, lowers the RDE's propulsive performance. Sato et al. [13] examined mixing processes in an RDE combustor with discrete fuel and air injections using three-dimensional numerical simulations. They observed that while fast injector recovery was crucial for continuous detonation propagation, steady recovery was equally important. Unsteady injector recovery intensified the undesired mixing of burned and unburned gases, leading to regions of autoignition ahead of the detonation wave. This premature deflagration was identified as the main source of loss in the pressure gain in an RDE.

Furthermore, with a detonation wave passing over a fueling injector at intervals below 0.1 ms, the impact of the wave on the injector performance, and conversely, the impact of the injector on the wave, remains largely unexplored [14]. Goto et al. [15] investigated the injection heights achieved by propellants entering an annular chamber. Their results showed that inconsistent injection heights could lead to instability and potentially extinguish the detonation reaction, causing severe vibrations. These challenges persist across all RDE configurations currently under consideration, underscoring the imperative for an efficient and reliable injector design. Elucidating the interdependent effects of the injector on the wave, and vice versa, is essential in the pursuit of an optimal design of fuel injectors for detonation engines.

In addition to the inherent technological challenges, uncertainties regarding the experimental conditions and numerical settings of previous work have introduced communication complexities among the research community. While some early numerical works lack experimental counterparts [16,17], and uncertainties in measurements hinder validation exercises [18], recent practices advocate for close collaboration between experimental and computational research. This entails using experimental data to validate numerical results and employing verified numerical codes to bolster the credibility of these results. Given the complexity of the flowfields involved, it is imperative to study the effects of operating conditions on injector performance in detonation engines, as well as to identify the optimal approach to represent these conditions in computational studies that can be validated against established experimental research. The present work aims to perform a comprehensive computational study of the valveless injector for detonation engine applications. The physical model considered is the recessed-cavity fluidic-valve injector measured by Peace et al. [11]. To find the conditions best representing the experimental data, three cases are considered and evaluated to choose the proper initial and boundary settings. The flow characteristics in the detonation tube and inside the injector are recorded and analyzed for each case to examine the injector performance.

The rest of the paper is organized as follows. Section 2 introduces the theoretical and numerical framework, including case descriptions and model validation and verification. The results and discussions are presented in Section 3, and the conclusions in Section 4.

2. Numerical Method and Physical Model

In detonation simulations, the timescale associated with chemical reactions is typically much smaller than that of flow processes. Therefore, transport effects such as viscosity and heat conduction can be ignored [19]. All cases in the paper are solved using the Euler conservation equations of mass, momentum, and energy, considering finite-rate chemical kinetics. To capture the multidimensional characteristics of detonation phenomena, three-dimensional computations are generally preferred. However, due to limitations in computational resources, the present work resorts to two-dimensional configurations instead. The suitability of the two-dimensional Euler equations in resolving detonation structures has been examined by Oran et al. [20]. According to their findings, the flowfields resolved using the Euler equations closely resembled those computed using the Navier–

Stokes equations, except for minor structures that have a negligible impact on the overall detonation structure. The governing equations are written in the following vector form

$$\frac{\partial \boldsymbol{Q}}{\partial t} + \frac{\partial \boldsymbol{E}}{\partial x} + \frac{\partial \boldsymbol{F}}{\partial y} = \boldsymbol{H} \tag{1}$$

where the dependent variable vector $\boldsymbol{Q}$, convective flux vectors $\boldsymbol{E}$ and $\boldsymbol{F}$, and source vector $\boldsymbol{H}$ are defined as

$$\boldsymbol{Q} = \begin{bmatrix} \rho \\ \rho u \\ \rho v \\ \rho e_t \\ \rho Y_i \end{bmatrix}, \boldsymbol{E} = \begin{bmatrix} \rho u \\ \rho u^2 + p \\ \rho uv \\ u(\rho e_t + p) \\ \rho u Y_i \end{bmatrix}, \boldsymbol{F} = \begin{bmatrix} \rho v \\ \rho uv \\ \rho v^2 + p \\ v(\rho e_t + p) \\ \rho v Y_i \end{bmatrix}, \boldsymbol{H} = \begin{bmatrix} 0 \\ 0 \\ 0 \\ 0 \\ \dot{\omega}_i \end{bmatrix} \tag{2}$$

where ρ, u, v, e_t, and p represent the density, axial velocity, vertical velocity, specific total energy, and pressure, respectively; Y_i and $\dot{\omega}_i$ are the mass fraction and mass production rate of species i, $i = 1, ns - 1$ and ns is the total number of species. The specific total energy, e_t, is calculated as

$$e_t = \sum_{i=1}^{ns} Y_i \left(\Delta h_{f,i}^0 + \int_{T_{ref}}^{T} C_{p,i}(T) dT \right) - \frac{p}{\rho} + \frac{(u^2 + v^2)}{2}$$

where $\Delta h_{f,i}^0$ is the enthalpy of formation of species i, and $C_{p,i}(T)$ is the specific heat at constant pressure evaluated with the NASA polynomials [21]. The pressure is evaluated using the equation of state for a perfect mixture,

$$p = \sum_{i=1}^{ns} p_i = \rho R_u T \sum_{i=1}^{ns} Y_i / MW_i$$

where MW_i is the molecular weight of species i and R_u is the universal gas constant. A system of nr elementary reactions can be represented as

$$\sum_{j=1}^{nr} \nu'_{ji} C_i \leftrightarrow \sum_{j=1}^{nr} \nu''_{ji} C_i, \; i = 1, \ldots, ns \tag{3}$$

where ν'_{ji} and ν''_{ji} are the stoichiometric coefficients of species i in the reactants and products of the jth elementary reaction ($j = 1, \ldots, nr$), and C_i is the concentration of species i in the mixture. The net mass production rate of species i from all the chemical reactions is determined as

$$\dot{\omega}_i = MW_i \cdot \sum_{j=1}^{nr} \left[\nu''_{ji} - \nu'_{ji} \right] \left\{ k_{jf} \prod_{i=1}^{ns} C_i^{\nu'_{ji}} - k_{jb} \prod_{i=1}^{ns} C_i^{\nu''_{ji}} \right\}$$

where k_{jf} and k_{jb} are the forward and backward reaction rate constants for the jth reaction. For each elementary reaction, k_{jf} is calculated using the empirical Arrhenius equation,

$$k_{jf} = A_j \cdot \exp\left(-E_{ja} / R_u T\right)$$

where A_j is a constant termed the preexponential factor and E_{ja} is the activation energy. The equilibrium constant of the j^{th} elementary reaction K_j, which is a function of temperature, is used to calculate k_{jb},

$$k_{jb} = k_{jf} / \mathrm{K}_j$$

In the current study, an eight-species, nineteen-step elementary mechanism [22] is employed to model the H_2-O_2 combustion. A second-order upwind scheme is used to solve the flow equations, and a multi-stage Runge–Kutta explicit transient formulation is

applied for temporal integration. To obtain time-accurate solutions, the time steps are fixed at values that satisfy the requirements imposed by the Courant–Friedrich–Lewy condition. All simulations in this study are carried out using the density-based solver for unsteady flows in Ansys Fluent 2020 R1. This solver has been extensively employed and validated for detonation research [23,24].

2.1. Case Descriptions

To reduce numerical uncertainty, simulations are first performed in a straight detonation tube. Figure 1 shows a schematic of the computational domain in the baseline case, consisting of a small ignition zone near the tube headend (A), and the remaining section of the detonation tube (B). The detonation wave is represented by the red line with an arrow indicating its propagation direction. The ignition and tube zones are abbreviated as "ignition" and "tube", respectively. The detonation tube has a total length, l_t, of 838 mm (33 inches) and a height, d_t, of 25 mm (1 inch). The length of the ignition zone, l_i, measures 2.5 mm (0.1 inches). The tube zone is initially filled with a premixed stoichiometric H_2-O_2 mixture at 1 atm and 300 K. The ignition zone is initialized with a mixture in chemical equilibrium at 35 atm and 3500 K. The equilibrium mixture includes H_2, H, O_2, O, OH, HO_2, H_2O_2, and H_2O predicted by the H_2-O_2 combustion mechanism [22]. These parameters reflect the state behind the detonation wave, eliminating the need to treat the deflagration-to-detonation transition.

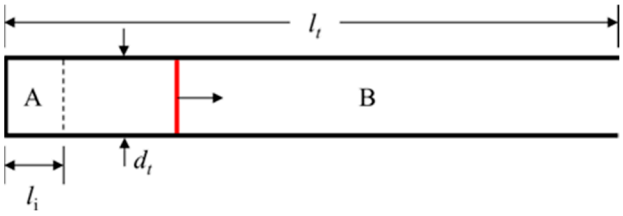

Figure 1. Schematic of the detonation tube, baseline case.

With the simple tube as the baseline case, a detonation tube-injector system is constructed. Figure 2 shows the configuration and dimensions of the system considered in the present work. The model is based on the PDE-mounted fluidic-valve injector that was experimentally measured by Peace et al. [11]. It consists of a detonation tube, representing the engine operating environment, and a recessed-cavity injector attached to the side of the tube. To facilitate the computational analysis, the entire domain is divided into four zones. The first two zones, denoted A and B, are carried over from the baseline case. The remaining two zones in the attached injector are consistent with the experimental setup: a narrow pipe open to the tube, labeled as zone C, and a cavity connecting to the propellant supply line, designated as zone D. The four zones are referred to as ignition, tube, orifice, and cavity, respectively. To ensure a well-established detonation wave approaching the injector, the injector centerline is placed a distance L_o of 114 mm (4.5 inches) downstream of the tube headend. Within the injector, the orifice has a length l_o of 46 mm (1.8 inches) and a diameter d_o of 6.3 mm (0.25 inches), and the cavity has a length l_c of 63 mm (2.5 inches) and a diameter d_c of 9.5 mm (0.375 inches).

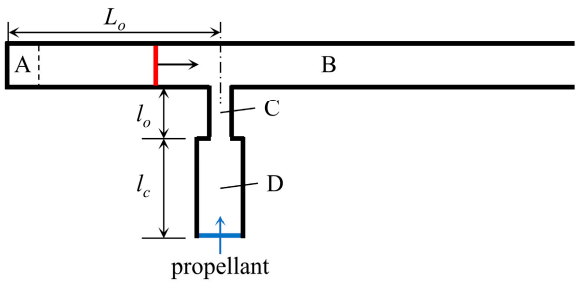

Figure 2. Schematic of the fluidic-valve injector attached to the detonation tube for Cases I–III.

To study the effects of injector operating conditions on the propagation of the detonation wave, three different sets of injector conditions are considered, as listed in Table 1. It is worth noting that in the experiments, the injector was supplied with air. To simplify the computational analysis, only the species included in the reaction mechanism are considered, and pure oxygen is used instead of air. In all three cases, the injector is initialized with still oxygen. In Cases I and II, the injector has an initial static pressure of 1.0 atm, while in Case III, the injector is pressurized to 5.1 atm (75 psi). The propellant injection condition at the cavity base is also varied among these three cases. In Case I, a choked flow from the supply line is assumed, and the cavity base is specified as a velocity inlet with a normal speed of 325 m/s, corresponding to the speed of sound in oxygen at 1 atm and 300 K. In Cases II and III, the velocity is not explicitly specified. Instead, the cavity base is set as a pressure inlet, with Case II having a static pressure of 5.1 atm and Case III having a total pressure of 5.1 atm, ensuring a propellant stream without explicitly assigning the velocity. It is worth noting that the boundary setup in Case III allows the propellant injection speed and flowrate to adjust as the pressure in the injector changes during the recovery process.

Table 1. Injector operating conditions.

Case	Initial Condition	Boundary Condition for Propellant Supply
I	oxygen, 1.0 atm	velocity inlet, 325 m/s
II	oxygen, 1.0 atm	pressure inlet, static pressure = 5.1 atm
III	oxygen, 5.1 atm	pressure inlet, total pressure = 5.1 atm

2.2. Model Validation and Verification

To minimize numerical uncertainty, a grid convergence study is performed in the baseline case. Four different grid levels are considered, with a refinement ratio of 1.5 in each coordinate. The aspect ratios of the computational cells are fixed at unity to prevent stretching effects. Note that the detonation cell width is about 1.5–2 mm in a stoichiometric H_2-O_2 mixture [25,26]. The mesh sizes at all the grid levels are smaller than this range to ensure a reasonable numerical resolution. Table 2 summarizes the total cell numbers and average cell sizes for all four levels.

Table 2. Numerical grids.

	Level 1	Level 2	Level 3	Level 4
number of cells, N	330,000	737,550	1,648,128	3,708,288
average cell size, in mm	0.25	0.17	0.11	0.08

The calculations start from the prespecified conditions at $t = 0$. Figure 3a shows the distributions of pressure gradient magnitude near the detonation front at $t = 70$ ms for the four different levels of resolution. The results from the Level 1 grid show the least detail. At the Level 2 grid, the cross-hatching pressure gradients caused by the expansion of the detonation cell wavelets appear, along with more details near the wave front. These cross-hatching pressure gradients serve as an approximation for the cellular structures observed in the soot-foil records of the maximum pressure footprints [27]. The flow structures become clearer in Levels 3 and 4, respectively. The thickness of the detonation shock front is determined by measuring the distance from the initial pressure rise to the peak pressure. As the refinement level increases, the shock thickness decreases from 1.07 mm in Level 1 and 0.71 mm in Level 2 to 0.49 mm in Level 3. Further mesh refinement results in a slight decrease to 0.38 mm in Level 4, suggesting the achievement of grid convergence.

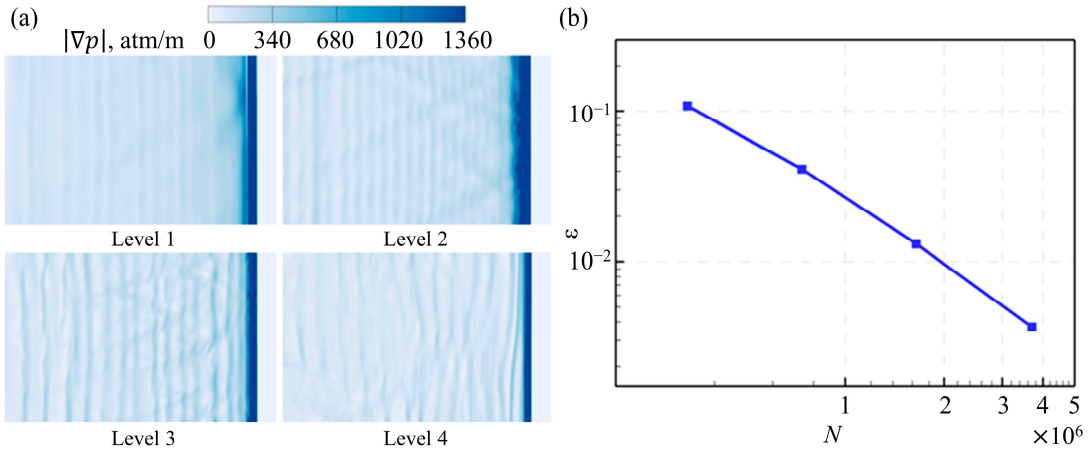

Figure 3. Grid convergence (**a**) distributions of pressure gradient magnitude near the detonation front; and (**b**) errors in the peak pressure as a function of cell numbers (baseline case).

Following Roache [28], grid convergence is further assessed using the grid convergence index (GCI) defined for two successive grids i and $i+1$, where grid $i+1$ is finer than grid i

$$GCI_{i,i+1} \equiv \frac{F_S \cdot |\varepsilon_{i,i+1}|}{r^{\Pi} - 1} \tag{4}$$

where F_S is the factor of safety and has a recommended value of 1.25 when three or more grids are used; $\varepsilon_{i,i+1} = |f_i - f_{i+1}|/f_i$ is the relative error between two grids; r is the grid refinement ratio, which is set to be 1.5 in the present work; and f is a flow property. The parameter Π is the order of convergence defined as

$$\Pi \equiv \frac{\ln[(f_1 - f_2)/(f_2 - f_3)]}{\ln r} \tag{5}$$

Taking the peak pressure across a detonation wave as the flow property, the respective values of f_1, f_2, and f_3 are measured as 18.9, 20.3, and 20.9 atm in the simulations using Levels 1–3 grids. The relative errors for each refinement are then calculated as $\varepsilon_{1,2} = 0.07$ and $\varepsilon_{2,3} = 0.03$. The order of convergence is found to be $\Pi = 2.1$, indicating a theoretically second-order solution. Consequently, the GCIs are determined as $GCI_{1,2} = 0.07$ and $GCI_{2,3} = 0.03$. A small GCI value suggests that the computation has low numerical uncertainty due to spatial discretization error. Additionally, the solutions should be within the asymptotic range, meaning that they should be obtained using a sequence of systematically refined grids over which the discretization error is reduced. The achievement of the asymptotic range is considered when

$$\frac{GCI_{1,2}}{r^{\Pi} \cdot GCI_{2,3}} \approx 1 \tag{6}$$

The calculated GCIs predict a value of 1.08, confirming the grid convergence. Using a nonlinear least squares regression technique, the asymptotic peak pressure across the detonation wave is determined to be 21.2 atm. The relative errors in the peak pressure are subsequently calculated as $\varepsilon = 0.10$, 0.04, 0.01, and 0.003 for mesh Levels 1, 2, 3, and 4, respectively. Figure 3b shows the relative errors in the peak pressure, ε, as a function of cell numbers, N, in a log–log scale. According to these results, the Level 3 grid is considered sufficiently reliable and is thus employed for the subsequent simulations.

Figure 4 shows profiles of pressure, temperature, and H_2 mass fraction, respectively, across the detonation wave for the Level 3 grid in the baseline case. As the detonation wave passes through the unburnt mixture, it compresses the gases and raises the static pressure to the value described by the von Neumann spike, which is over 20 atm in the baseline

case. The mixture temperature also rises sharply due to aerodynamic heating from the normal shock wave. The combined elevated temperature and pressure creates the necessary conditions for autoignition of the mixture. As intermediate reactions occur, radicals are generated, leading to explosive reactions and the release of heat at a substantially higher rate compared to deflagration. Key detonation characteristics, such as wave propagation speed and chemical heat release rate, can be estimated at the Chapman–Jouguet (C-J) condition. In Figure 4, the C-J point is identified by the location at which the H_2 mass fraction decreases to the equilibrium value in the burnt mixture. At the C-J point, the mixture temperature measures 3682 K, and the pressure is 18.1 atm. These values align with the theoretical prediction for a stoichiometric H_2-O_2 detonation at an initial pressure of 1 atm [25].

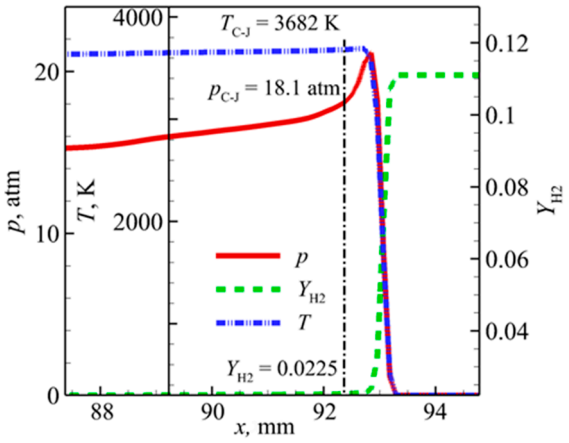

Figure 4. Reaction processes across the detonation wave (baseline case, Level 3 grid).

3. Results and Discussion

The flowfield within the detonation tube-injector assembly exhibits significant unsteadiness. To illustrate the overall development of the flow, pressure history is recorded at three probes whose locations correspond to those of the pressure transducers used in the experiments. To ensure a fully developed detonation wave and avoid headend effects, the three pressure transducers (PCB) used in the experiments by Peace et al. [11] are replicated numerically using pressure probes, as shown in Figure 5: (1) PCB 5 is placed inside the tube at a distance, L_5, of 61 mm (2.4 inches) ahead of the injector centerline; (2) PCB B is positioned at a distance, L_B, of 72 mm (2.85 inches) below the wall orifice inside the injector cavity; and (3) PCB T is located at a distance, L_T, of 95 mm (3.75 inches) below the wall orifice and 15 mm (0.55 inches) above the cavity base. It is important to note that all the pressure transducers in the experiments were located at the walls, while in the simulations, PCB 5 is located along the tube centerline and PCB B and PCB T are located at the injector centerline. Figure 5 shows the pressure histories at the three probes from both numerical and experimental studies. The time coordinates are adopted from the experimental study [11]. To facilitate comparison, the initial pass of the detonation wave at PCB 5 has been aligned by shifting the numerical results forward by 55 μs. Note that in the simulations, PCB 5 is located 53 mm (2 inches) closer to the orifice centerline than that in the experiments. According to a ZND-based theoretical analysis, the detonation wave speed is estimated to be approximately 2780 m/s, suggesting a travel time of 19 μs over a 53 mm distance. Therefore, the numerical results at PCB B and PCB T are shifted forward by 36 μs.

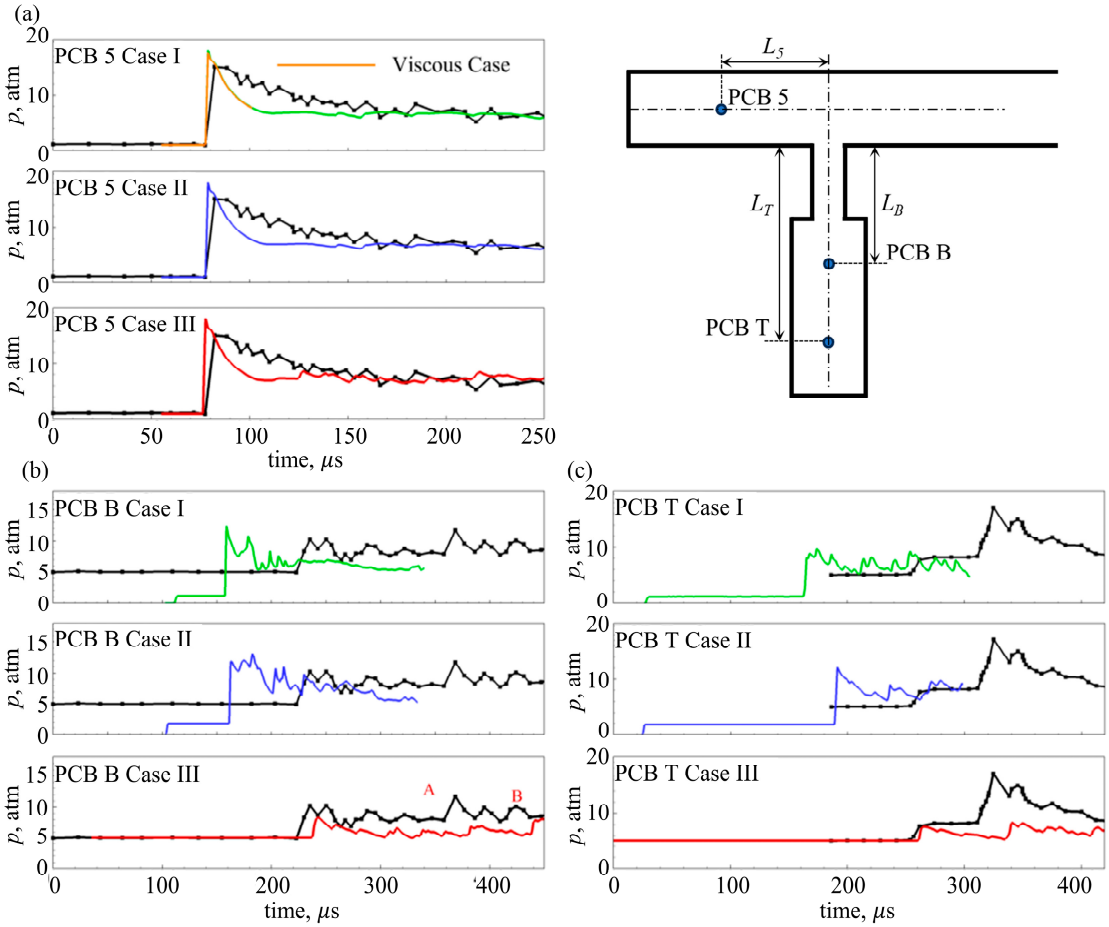

Figure 5. Experimental and numerical pressure traces: (**a**) PCB 5, (**b**) PCB B, and (**c**) PCB T. Experiments in black; Case I in green; Case II in blue; Case III in red.

Figure 5a compares the pressure history at PCB 5 immediately upstream of the injector orifice. In all simulations, the pressure decreases rapidly following the initial spike, while the decrease is more gradual in the experiment. One possible explanation for this difference is that a two-dimensional duct is modeled in the simulations, whereas the experiment was conducted in a three-dimensional tube. The inclusion of a third dimension in the experiment provides the flow with additional capacity to store energy and resist change, relieving the post-detonation pressure relaxation. Another factor that may contribute to the difference in pressure decrease trends is the method employed for simulating chemical reactions. The numerical model incorporates finite-rate chemistry, which can result in variations in energy release rates compared to the experimental conditions. These differences in the energy release rates may lead to discrepancies in the pressure evolution behind the detonation front. Since the injector setups do not affect the flow within the detonation tube, the pressure evolutions of the numerical cases exhibit similarities.

After the detonation wave diffracts into the flush-wall opening, it degenerates into a shock wave that propagates through the orifice and expands into the cavity. Figure 5b shows the pressure history at PCB B, inside the cavity. Compared to the experimental results, the pressures in Cases I and II start with lower values and rise to similar spikes upon the arrival of the shock wave. In Case III, the pressure initially matches the experiment, but it shows a much smaller increase after the shock wave, suggesting different wave diffraction processes at the orifice. The Case III results also suggest the impact of injector conditions on the shock wave magnitude and propagation speed. After the initial shock wave traverses the cavity, it reflects off the cavity base and induces a second pressure spike. The pressure spike caused by the arrival of this reflected shock wave is denoted by Marker

A in the experiment and Marker B in Case III. In Cases I and II, with low propellant injection pressures, the reflected expansion waves are not recorded during the simulation window. It is worth noting that the abrupt geometric contraction from the cavity to the orifice forms a partial barrier that interferes with the advection of mass and momentum inside the injector and causes additional wave reflections, as indicated by the uneven pressure evolution in both the experimental and numerical results. Considering the wave arrival time and overall evolution of the experiment, Case III shows better agreement than Cases I and II.

To illustrate the unsteady motion near the propellant supply line, Figure 5c compares the pressure history at PCB T close to the cavity base. Until the first pass of shock waves at t = 270 μs, Case III shows good agreement with the experiment, with the same pre-shock pressure and a comparable pressure jump behind the initial shock wave. Immediately after passage of the shock wave, the pressure remains constant in the experiment, but shows a steady drop in Case III. Upon the arrival of the first reflected shock, denoted by Marker C at around t = 320 μs in the experiment and Marker D at t = 340 μs in Case III, PCB T encounters another sharp pressure jump, due to its proximity to the cavity base. Since the pressure increase behind each shock affects the recovery time of the injector in supplying fresh propellant, it will be important to obtain a quantitative description of the shock motions and achieve a better estimate of the injector interruption time in future simulations. Since Case III best represents the experimental work, it is examined in detail in the following section.

3.1. Detonation Wave Diffraction at the Injector Orifice

The highly unsteady wave behaviors inside the injector begin with the diffraction of the detonation wave into the flush-wall orifice. Figure 6a shows, to illustrate a concept, a shock diffracting into a still zone at an unconfined opening. As the detonation wave passes the opening, expansion waves start to emanate at the corner, O. The resulting disturbance propagates at the local sound speed c while being transported downstream at the post-shock particle speed of u, intercepting the detonation wave front and inducing curvature in its otherwise planar front. At an instant Δt after the detonation wave passes O, the lower part of the detonation front AB has assumed a curved shape, while the upper part BC remains planar. Adapted from Skews's geometric construction for non-reacting diffracting shocks [29,30], the angle α between the disturbance trajectory and the normal of the incoming detonation wave can be determined with the formula

$$\tan\alpha = \frac{v}{D} = \frac{\sqrt{c^2 - (D-u)^2}}{D} \tag{7}$$

where D is the undisturbed detonation wave speed and v is the propagation speed of the interaction point B on the wave front. The current concept is depicted in Figure 6b, where the flush-wall orifice is a confined opening. The continuous wave front bifurcates at the rear corner of the orifice: the majority of the lower part enters the injector, while the remaining curved portion, combined with the undisturbed planar section, continues to propagate downstream in the tube. This orifice is not a stagnant zone; instead, transverse flows exit the orifice due to either the velocity (Case I) or pressure (Case III) inlet at the injector base. The resulting shock diffraction process is illustrated in Figure 7a–c.

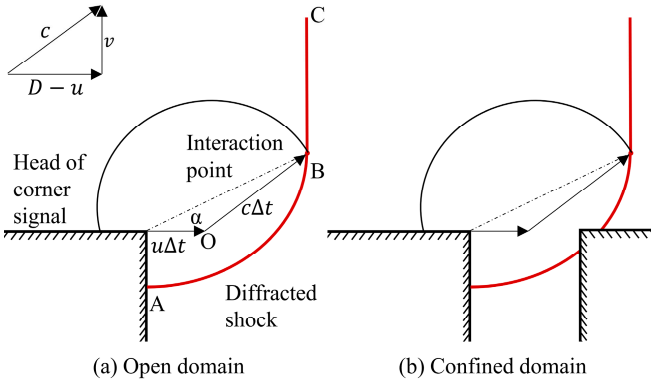

Figure 6. Schematic of a shock diffracting into a still zone: (**a**) open domain (adapted from [18]) and (**b**) confined domain.

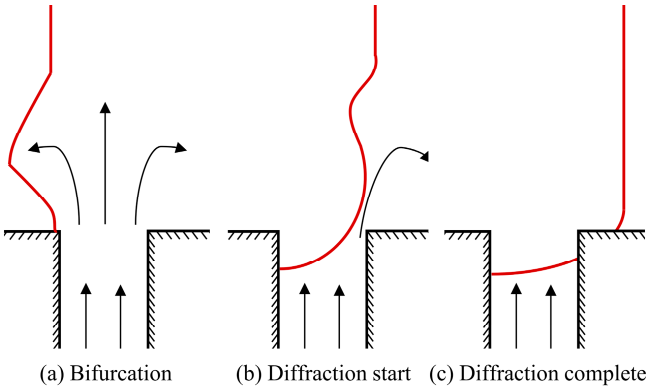

Figure 7. Schematic of a shock diffracting into a transverse flow.

Figure 8 shows the detonation wave diffraction process in Case II, where the injector has the same initial pressure as the detonation tube, and the zone inside the injector is initially still. In this configuration, the results are similar to those of earlier research conducted on detonation diffraction [31,32]. In Figure 8c, an expansion region forms at the portion of the detonation wave entering the injector, as the leading shock decouples from the reaction zone. As the detonation wave passes the orifice, most of it is unaffected, and only the small near-wall portion comprising the expansion region is pushed into the injector by the high-pressure hot product behind it. By locating the interaction point at multiple time steps as the detonation crosses the injector, the angle α is found to be 17 deg. A known detonation velocity of 2800 m/s and C-J point sonic speed of approximately 1460 m/s results in a corner signal propagation velocity of 1590 m/s into the burnt region behind the detonation. The curved diffracted shock front is confined by the orifice and divided into two parts at the rear corner; one part continues to move downstream in the detonation tube, while the other part penetrates the orifice and initializes the highly unsteady wave motions inside the injector. A curved shock is observed inside the injector in Figure 8d. Propagation velocity can be used to determine injector spacing and ensure that a recovering injector downstream is minimally affected by the wave processes. The description of wave curvature will contribute to better understanding the potential for reinitiation during diffraction, to be elaborated in a later section.

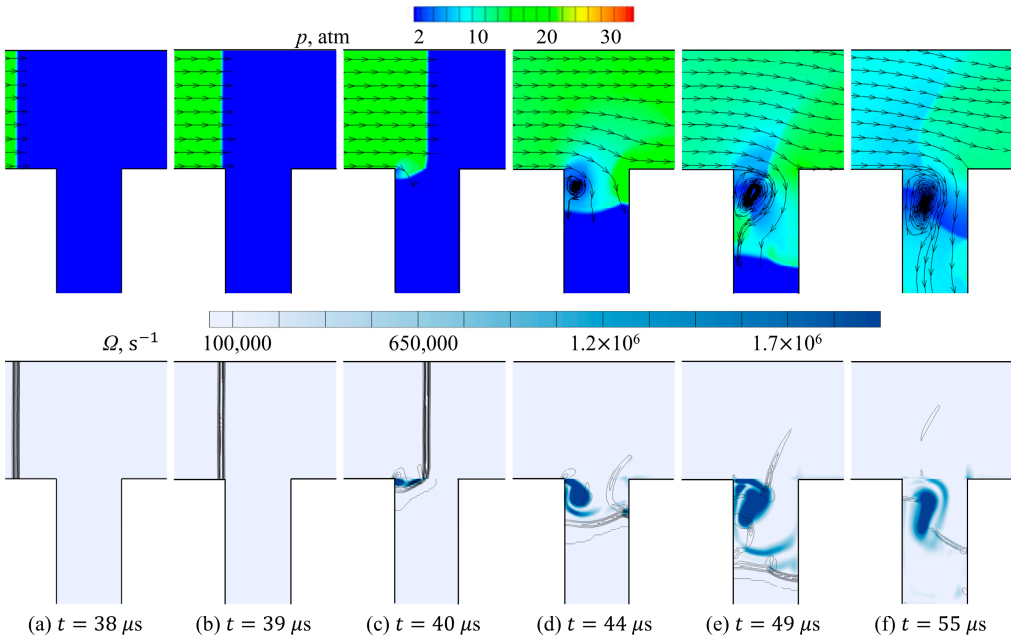

Figure 8. Distributions of pressure and vorticity magnitude with streamlines near the injector orifice (Case II).

Figure 9 shows, using both pressure and vorticity magnitude contours, the diffraction process in Case III. Upon initiation of the simulation, the pre-pressurized injector assembly experiences an initial transverse propellant flow, with an instantaneous propellant mass flow rate of 50 g/s, into the detonation tube. This mass flow rate persists as the detonation wave approaches the injector, only to be interrupted upon the passage of the wave. In Figure 9a, the expansion of propellant from the pressurized injector leads to flow recirculation near the orifice. In Figure 9b, as the detonation wave approaches the orifice, it interacts with the recirculation region, causing deceleration of the lower part of the wave. Consequently, the wave front splits into two parts, with the undisturbed upper part propagating down the detonation tube. As shown in Figure 9c,d, the lower part diffracts into the injector and its behavior downstream of the orifice closely resembles the shock diffraction process sketched in Figure 7. Additionally, the wave front is further deformed by an expansive disturbance emanating from the leading corner. In Figure 9e, the diffracted curved shock front divides into two parts at the rear corner of the orifice: one part moves downstream in the detonation tube, interacts with the rear recirculation zone, and pushes the vorticity downstream; the other part penetrates the orifice and distorts the otherwise steady flow inside the injector, initializing highly unsteady wave motions. A vortical structure is formed just below the orifice, as visualized by the distributions of pressure and vorticity magnitudes in Figure 9d–f. This vortex reduces the transverse momentum and prevents excessive penetration of the hot burnt products into the injector. Since the injector is filled with fresh propellant, the diffracted detonation wave entering the injector loses its reaction zone and degenerates into a shock wave.

Note that in Case I, the injector is initialized with still propellant, and the velocity inlet boundary condition is activated only when the simulation starts. As a result, transverse flow is not established when the detonation wave reaches the wall orifice. Consequently, the wave diffraction process in Case I resembles that in Case II and is not shown here. The effect of the injector's initial pressure is demonstrated by comparing Cases II and III. In Case II (Figure 8), the propellant plume and the accompanying shear layers are absent from the detonation tube, eliminating the wave bifurcation observed in Figure 9b–d. The pressure difference across the diffracting shock is larger in Case II than in Case III, causing the shock to propagate into the injector at a faster speed (Figure 8e,f). Furthermore, although vorticity is generated near the orifice in Case II, the interaction between the shock

wave and vorticity is weakened compared to that in Case III, leading to stronger shock waves and larger pressure spikes within the injector, as shown in Figure 5b.

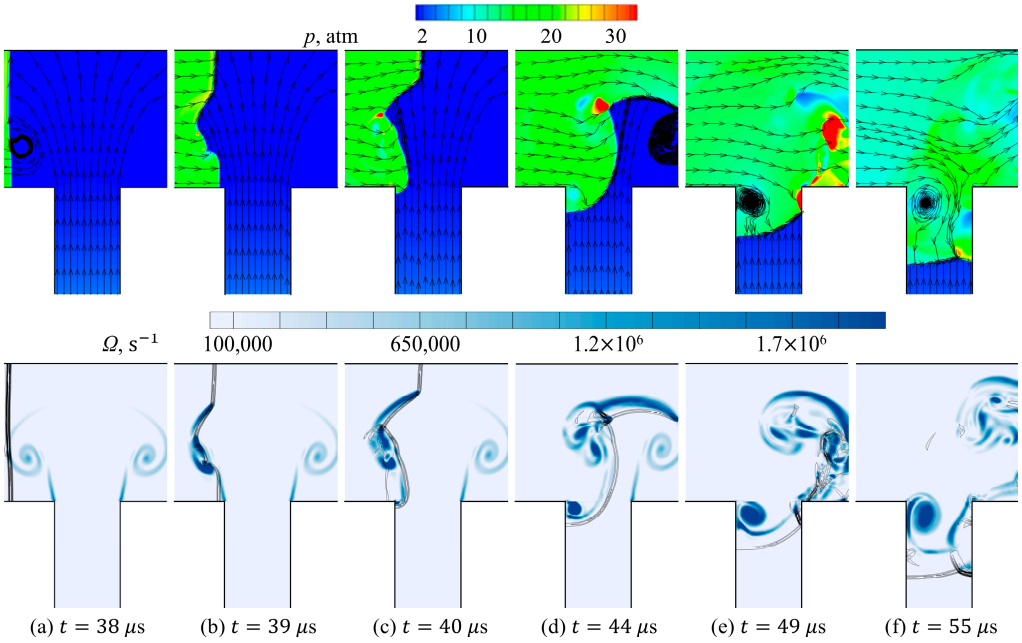

Figure 9. Distributions of pressure and vorticity magnitude with streamlines near the injector orifice (Case III).

3.2. Shock Wave Dynamics Inside the Cavity

As shown in Figure 2, each fluid-valve injector is comprised of two parts: the orifice (zone C), exposed to the detonation tube, and the cavity (zone D), attached to the propellant plenum. The orifice is connected to the cavity through an abrupt area expansion. Shock motions in the orifice region are strongly influenced by the detonation wave diffraction at the flush-wall opening. The first shock wave reflection off the opposing orifice wall is followed by a series of reflections between the two orifice walls. The result is an undulation of the shock wave front, with the leading edge fluctuating between the left and right walls. The fluctuations are attenuated as the shock wave approaches the expansion into the cavity. When it reaches the cavity expansion, the shock wave resembles a normal shock, with no visible fluctuations along the wave front.

As a shock wave propagates further into the injector and towards the cavity base, it expands at the cavity entrance, interacts with the surrounding walls, and reflects at the gaseous interface between the cavity flow and the incoming propellant stream. The wave motions and residence times inside the cavity are of critical importance in determining the propellant injection efficiency and injector performance. Figure 10 shows the distributions of pressure and transverse velocity inside the cavity in Case I. Since the injector is initially filled with still fluid and the velocity inlet boundary condition at the cavity base takes time to update the injector flowfield, the detonation wave diffracts into the orifice and enters the cavity without encountering the opposing flow from the injected fluid. In Figure 10(b1), the shock wave travels downward at approximately 773 m/s. The upward propellant flow from the velocity inlet boundary has a velocity of 200 m/s. After the shock wave collides with the propellant stream, the pressure increases significantly in Figure 10(a2) and the velocity is reduced to about 550 m/s, as shown in Figure 10(b2), keeping a constant velocity as shown in Figure 10(b3) until it reflects off the cavity base.

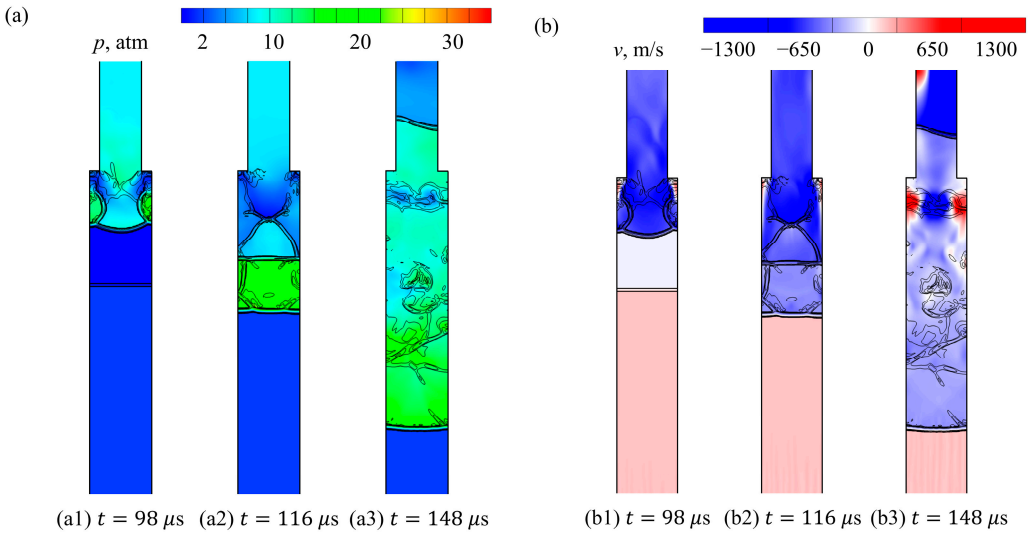

Figure 10. Distributions of (**a**) pressure and (**b**) transverse velocity inside the cavity, overlaid by the isoline of pressure gradient (Case I).

Figure 11 shows the distributions of pressure gradient magnitude for three cases at three instants: when the shock wave enters the cavity, transverses inside the cavity, and reflects off the cavity base. The streamlines in Figure 11 are generated from lines spanning the width of the cavity section at three locations: top at $y = -47$ mm from the orifice entrance, middle at $y = -79$ mm, and at the base of the injector $y = -109$ mm. Fuel flow is visualized by the uniform upward streamlines from the injector base in the early images of each case. The fuel velocity varies in the three cases: 325 m/s for the velocity inlet in Case I, 469 m/s for the static pressure inlet in Case II, and approximately 0.5 m/s in the pressurized cavity for the total pressure inlet in Case III. Figure 11a shows the results from Case I. Immediately after the incoming shock wave enters the cavity, it expands due to the abrupt area change, and the resultant overexpanded flow is incident to the wall, inducing recompression and secondary shock waves that interact and merge with the primary shock wave, as marked by the streamlines and pressure gradient contours at t = 98.75 μs. The resultant shock wave travels at an estimated speed of 660 m/s before it is slowed down by a collision with a pressure wave from the velocity inlet. It is approximately 90 mm into the injector at t = 153.75 μs. Vortical structures appear near the orifice–cavity joint because of flow expansion. Note that the high-pressure gradients near the cavity base result from the velocity inlet boundary condition. At about t = 260 μs, the shock wave reaches the cavity base, acting as a pressure boundary to the wave reflection, causing a series of expansion waves emerging from the inlet shortly afterward. No reflected pressure spikes are formed in Case I, as observed in Figure 5c.

Figure 11b shows the cavity flowfield in Case II. Similar to Case I, the incoming shock wave enters the cavity at t = 98.75 μs, inducing flow expansion, shock wave interactions, and recombination near the wall. The resultant shock wave travels at a slightly higher speed of 680 m/s toward the cavity base. Since the propellant supply has a pressure higher than that in the initial injector flow, compression waves stem from the cavity base and collide with the incoming shock wave. These shock interactions cause a large reduction in the wave speed, leading to a smaller shock penetration into the cavity at t = 155 μs than in Case I. Furthermore, as the shock wave reaches the cavity base, where it encounters higher pressure than in Case I, it reflects off the injector base, at t = 283.75 μs.

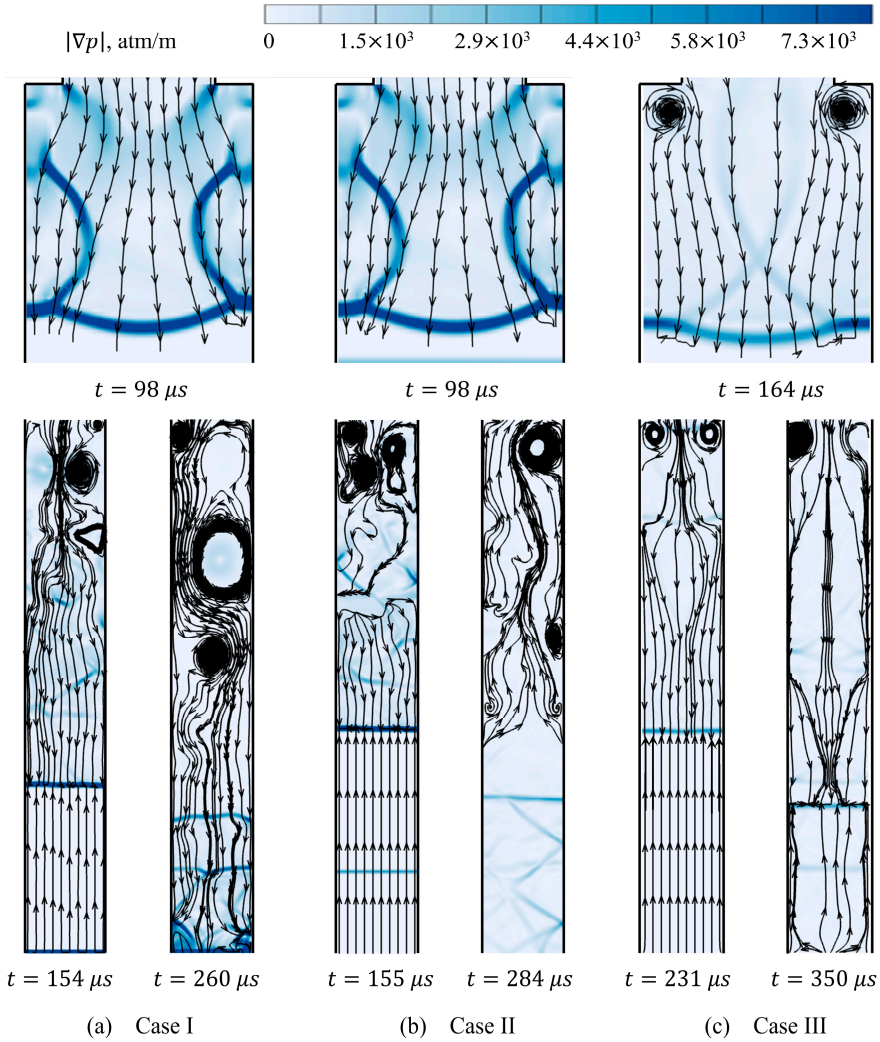

Figure 11. Distributions of pressure gradient magnitudes inside the cavity: near the orifice–cavity joint (**top row**) and close to the cavity base (**bottom row**).

The scenario in Case III is noticeably different, as shown in Figure 11c. Compared to Cases I and II, the injector in Case III is initialized to a much higher pressure. Due to the detonation wave and propellant plume interaction outside the flush-wall orifice, the incoming shock wave enters the injector at a lower speed of 400 m/s. As it expands into the cavity around t = 163.75 µs, its strength is further reduced, exhibiting much milder dynamics near the orifice–cavity joint. The pressure gradient magnitudes are significantly lower than those in Cases I and II throughout the cavity, indicating that a pressurized injector may facilitate steady propellant injection and mitigate the intermittent pressure pulses from the propellant supply line. The relative uniformity of the injector flowfield, and the close similarity of the pressure readings to the experimental results, make Case III the optimal condition for further analysis of injector operation.

3.3. Evolution of Contact Surfaces

As the shock wave enters the injector, it is followed by the hot detonation products. A phenomenon of particular interest is the contact surface forming between the burnt detonation products and the fresh propellant. Assuming negligible diffusive effects, as modelled by the current inviscid flow solver, the contact surface travels in the injector for some time and then ejects from the wall orifice. The residence time of the contact surface inside the injector is a critical factor in determining the recovery time required for the injector to resume fresh supply of propellant [9,33]. In the present study, the temporal

evolution of species mass fraction and temperature distribution is studied to deduce the motion of contact surfaces.

Figure 12 shows the distribution of OH mass fraction superimposed by the isolines of density gradient magnitude $|\nabla\rho| = 10\ \mathrm{kg/m^4}$ for Case III. After the shock diffraction into the orifice, the shock wave travels against a propellant flow that moves at approximately 185 m/s. The separation of the shock wave from the detonation products is first captured in Figure 12a. The shock wave traced by the isolines of density gradient magnitude significantly outpaces the burnt products in Figure 12b and reaches the orifice–cavity joint at approximately t = 136 µs in Figure 12c. After accounting for the opposing local flow velocity, the shock wave has an average velocity of approximately 450 m/s. The opposing flow also slows down the flow of burnt products, leading to a velocity of about 60 m/s at the leading edge of the contact surface. At t = 491 µs, the reflected shock wave propagates toward the orifice and the contact surface ceases to move further into the cavity. As shown in Figure 12, the contact surface reaches about 35 mm into the orifice before reversing back toward the detonation tube at approximately 120 m/s. The first sign of contact surface ejection is observed at t = 600 µs in Figure 12f. The penetration of contact surfaces into the injector could be further reduced by changing the geometric parameters of the injector; this will be addressed in future research.

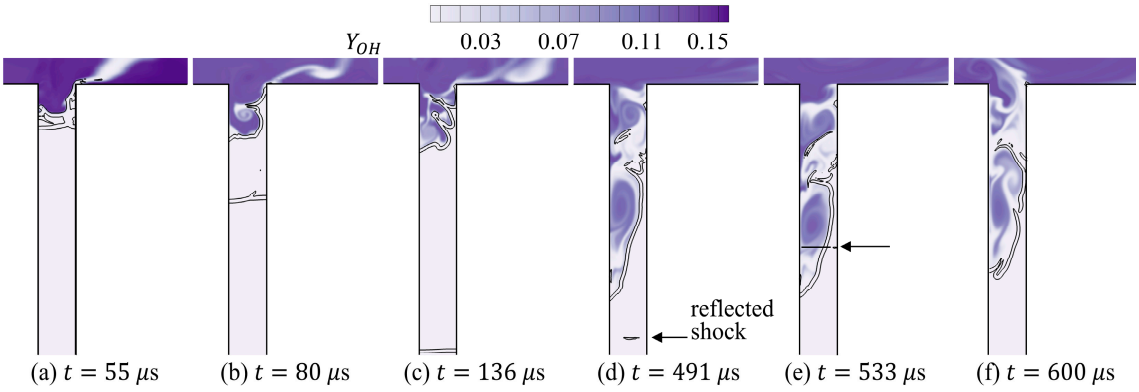

Figure 12. Distributions of OH mass fraction inside the injector superimposed by the isolines of density gradient magnitude (Case III). Arrow indicates location of reflected shock.

Figure 13 shows the temperature distributions at the same instants as in Figure 12. In Figure 13a, the detonated mixture trailing the decoupled shock front has a temperature of about 3400 K at the flush-wall opening. The undisturbed propellant flow inside the injector has a temperature of 300 K. In Figure 13b–d, the shock front sweeps through the orifice and compresses the propellant flow to around 400 K. As the detonated mixture spreads into this shocked but unreacted propellant, the temperature near the contact surface is about 1800 K. In Figure 13d–f, because of the reflected shock, the hot mixture starts to retreat to the detonation tube and the orifice zone starts to refill with fresh propellant. Since the local fuel–air equivalence ratio is well above the flammability limit, exothermic reactions are not anticipated inside the orifice zone. Nonetheless, the temperature and mixture composition inside the orifice are critical factors in accounting for potential autoignition in the propellant flowpath. Further analyses, especially considering diffusion processes, are needed to explore the temperature distributions and evolution.

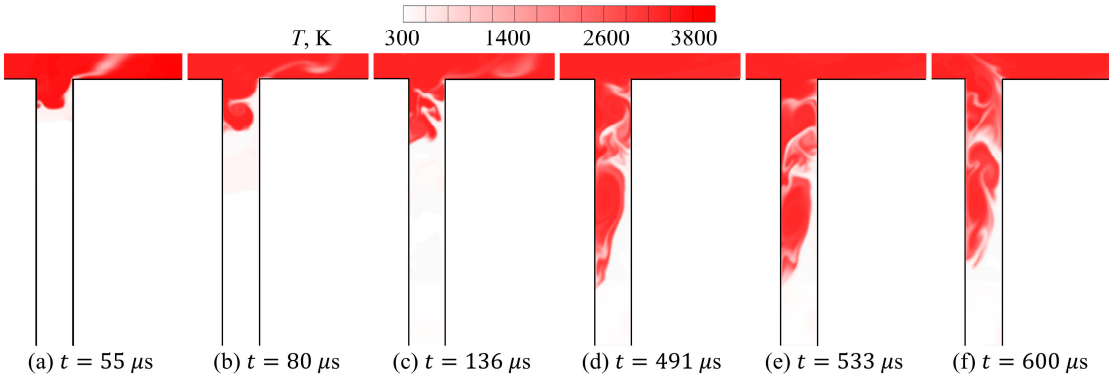

Figure 13. Temperature distribution inside the injector superimposed by the isolines of density gradient magnitude (Case III).

3.4. Potential for Reinitiation

In previous studies on detonation transition criteria in tubes, Peraldi et al. [34] discovered that a minimum ratio of 13 between the tube diameter and the detonation cell width is necessary for a successful transition from deflagration to detonation. In the current configuration, the detonation cell width is 2.08 mm. The ratios of the tube diameter to the cell width in the orifice and cavity zones are approximately 3.05 and 4.58, respectively. Consequently, the likelihood of a deflagration-to-detonation transition occurring inside the injector is low [25]. If any detonation waves were to enter the injector, they would have to originate from reinitiation during the diffraction phase.

When a detonation wave diffracts into a stagnant zone, potential reinitiation sites are found at the hot spots on the curved diffracted wave at the sharp opening. These hot spots have the potential to ignite transverse detonation waves that travel along the wave until they reflect off one of the side walls [35]. If this were to occur, the detonation wave could penetrate throughout the rest of the injector. However, generating transverse detonation waves in the current model is challenging since the detonation diffraction process is confined to a limited duration over a restricted opening.

Furthermore, the pressurized injector scenario poses an additional challenge for reinitiating detonation inside the injector. Li et al. [36] studied detonation wave diffraction into a supersonic crossflow. They found that introducing a supersonic crossflow increases the likelihood of reinitiation in unstable detonations with irregular cellular structures. In practical applications that employ air as the oxidizer, the irregular cellular structure increases the chances of reinitiation. When simulating a subsonic injector flow, the additional pressure from the incoming flow can increase the potential for reinitiation. To prevent detonation reinitiation in both pressurized and unpressurized cases, a possible approach is to modify the pathway of the detonation wave as it turns into the orifice. Wang et al. [37] explored detonation diffraction around obstacles of semicircular, triangular, and rectangular shapes. They established a correlation between the likelihood of reinitiation and the ratios of obstacle size (radius for semicircular obstacles, and length for triangular and rectangular obstacles) to induction length. They discovered that for semicircular obstacles, the supercritical regime with a continuously coupled shock-reaction front occurs at ratios larger than 100. As the ratios decrease, the critical regime is encountered, characterized by successive shock-reaction front decoupling. Ratios below 12.5 lead to subcritical diffractions, where the leading shock decouples from the reaction front. Apart from obstacle size, obstacle shape significantly influences the regime distributions. In the case of rectangular and triangular obstacles, the subcritical regime arises when the upstream side of each shape is smaller than the characteristic reflection length [38,39]. Changing the lip geometry at the orifice entrance could leverage the subcritical regime and restrict reinitiation generated at the upstream orifice rim. Further research is needed to explore these design changes.

4. Conclusions

The present study describes a comprehensive numerical investigation of the instantaneous flowfield inside a recessed-cavity fluidic-valve injector attached to a detonation tube. To verify the computational framework and determine an appropriate mesh size, a baseline case is modeled with a straight detonation tube, and a grid independence study is performed using four different mesh resolutions. Based on an evaluation of the detonation wave structures, thicknesses, and computation times, the Level 3 grid is selected for the subsequent computations.

The computational results on the assembly of the detonation tube and injector are found to be notably affected by the numerical setup. To account for the effects of injector operating conditions and to accurately represent the experimental settings, three cases (I, II, and III) are simulated, each featuring different initial injector conditions and inlet setups. A comparison of the pressure data obtained from the experimental work reveals that Case III, which has an initially pressurized injector and a total pressure inlet boundary condition at the cavity base connecting to the propellant supply, shows the best agreement.

The primary focus of this study is to investigate key flow behaviors, including the diffraction of the detonation wave from the detonation tube into the flush-wall orifice, the dynamics of shock waves inside the cavity, and the penetration of the contact surface separating the burnt and unburnt gases into the injector. In Case III, the collision between the longitudinally travelling detonation wave and the transverse propellant stream leads to the bifurcation of the detonation wave ahead of the orifice. One portion of the wave expands in the tube, while the other part enters the orifice, resulting in the formation of a recirculation zone and vortical structures. The latter degenerates into a shock wave inside the injector, propagating towards the cavity base and creating a series of shock wave motions and pressure spikes that are in good agreement with the experimental results. The shock waves, together with their associated flow structures, interact with the stream of fresh propellant in the orifice, causing a deceleration of the contact surface. Consequently, the penetration of the contact surface into the injector is limited, and the recovery time required for the injector to supply fresh propellant is reduced. Further research is necessary to explore the influences of injector geometry on detonation wave diffraction, shock wave propagation, and the interruption of the propellant supply.

Author Contributions: Conceptualization, L.Z.; methodology, J.C.S. and L.Z.; software, J.C.S. and L.Z.; validation, J.C.S.; formal analysis, J.C.S.; investigation, J.C.S. and L.Z.; resources, J.C.S. and L.Z.; data curation, J.C.S.; writing—original draft preparation, J.C.S. and L.Z.; writing—review and editing, J.C.S. and L.Z.; visualization, J.C.S.; supervision, L.Z.; project administration, L.Z.; funding acquisition, L.Z. All authors have read and agreed to the published version of the manuscript.

Funding: This research was funded by the American Chemical Society Petroleum Research Fund under Grant No. PRF #65447-DNI9. And the article processing charge was funded by the University of Texas at Arlington.

Data Availability Statement: The datasets presented in this article are not readily available because the data are part of an ongoing study. Requests to access the datasets should be directed to the corresponding author.

Acknowledgments: The authors would like to express their gratitude to ANSYS® for providing Academic Research Mechanical Licenses and to Cadence® for providing Fidelity Pointwise. Acknowledgement is also made to the donors of the American Chemical Society Petroleum Research Fund for support of this research.

Conflicts of Interest: The authors declare no conflict of interest.

Nomenclature

Symbols	
A	preexponential factor
c	speed of sound
D	detonation wave speed
d	diameter
E_a	activation energy
e_t	specific total energy
F_S	convergence factor of safety
f	flow property
l	length
M	Mach number
N	number of cells
ns	number of species
p	pressure
R_u	universal gas constant
r	grid refinement ratio
T	temperature
t	time
u, v	velocity components
x, y	spatial coordinates
Y	mass fraction
α	angle between disturbance trajectory and detonation wave normal
ε	relative error
Π	order of convergence
ρ	density
Ω	vorticity magnitude
$\dot{\omega}$	mass production rate of reactants
Subscripts	
c	property of cavity
$C\text{-}J$	Chapman-Jouguet condition
i	index of nominal species
i	property of injector
o	property of orifice
t	property of detonation tube

References

1. Kailasanath, K. Review of Propulsion Applications of Detonation Waves. *AIAA J.* **2000**, *38*, 1698–1708. [CrossRef]
2. Lu, F.K.; Braun, E.M. Rotating Detonation Wave Propulsion: Experimental Challenges, Modeling, and Engine Concepts. *J. Propuls. Power* **2014**, *30*, 1125–1142. [CrossRef]
3. Pandey, K.M.; Debnath, P. Review on Recent Advances in Pulse Detonation Engines. *J. Combust.* **2016**, *2016*, 4193034. [CrossRef]
4. Roy, G.D.; Frolov, S.M.; Borizov, A.A.; Netzer, D.W. Pulse Detonation Propulsion: Challenges, Current Status, and Future Perspective. *Prog. Energy Combust. Sci.* **2004**, *30*, 545–672. [CrossRef]
5. Gejji, R.M.; Buschhagen, T.; Slabaugh, C.D. Occurrence of Rotating Detonation Waves in a Jet Stabilized Combustor with Premixed Injection. *J. Propuls. Power* **2021**, *37*, 645–649. [CrossRef]
6. Schwer, D.A.; Kailasanath, K. Towards Non-Premixed Injection Modeling of Rotating Detonation Engines. In Proceedings of the 51st AIAA/SAE/ASEE Joint Propulsion Conference, Orlando, FL, USA, 27–29 July 2015.
7. Fan, L.Z.; Shi, Q.; Zhi, Y.; Nie, W.S.; Lin, W. Experimental and Numerical Study on Multi-Wave Modes of H_2/O_2 Rotating Detonation Combustor. *Int. J. Hydrogen Energy* **2022**, *47*, 13121–13133. [CrossRef]
8. Han, J.; Bai, Q.; Zhang, S.; Wu, M.; Cui, S.; Chen, H.; Weng, C. Experimental Study of H_2/Air Rotating Detonation Wave Propagation Characteristics at Low Injection Pressure. *Aerosp. Sci. Technol.* **2022**, *126*, 107628. [CrossRef]
9. Braun, E.M.; Balcazar, T.S.; Wilson, D.R.; Lu, F.K. Experimental Study of a High-Frequency Fluidic Valve Fuel Injector. *J. Propuls. Power* **2012**, *28*, 1121–1125. [CrossRef]
10. Lu, F.K.; Jensen, D. Potential Viability of a Fast-Acting Micro-Solenoid Valve for Pulsed Detonation Fuel Injection. In Proceedings of the 41st Aerospace Sciences Meeting and Exhibit, Reno, NV, USA, 6–9 January 2003.
11. Peace, J.T.; Joshi, D.D.; Lu, F.K. Experimental Study of High-Frequency Fluidic Valve Injectors for Detonation Engine Applications. In Proceedings of the 52nd Aerospace Sciences Meeting, National Harbor, MA, USA, 13–17 January 2014.

12. Fujii, J.; Kumazawa, Y.; Matsuo, A.; Nakagami, S.; Matsuoka, K.; Kasahara, J. Numerical Investigation on Detonation Velocity in Rotating Detonation Engine Chamber. *Proc. Combust. Inst.* **2017**, *36*, 2665–2672. [CrossRef]
13. Sato, T.; Chacon, F.; White, L.; Raman, V.; Gamba, M. Mixing and Detonation Structure in a Rotating Detonation Engine with an Axial Air Inlet. *Proc. Combust. Inst.* **2021**, *38*, 3769–3776. [CrossRef]
14. Redhal, S.C.; Burr, J.R.; Yu, K. Injector Flowfield-Detonation Wave Interaction in Unwrapped RDE Channel. In Proceedings of the AIAA Propulsion and Energy 2019 Forum, Indianapolis, IN, USA, 19–22 August 2019.
15. Goto, K.; Nishimura, J.; Kawasaki, A.; Matsuoka, K.; Kasahara, J.; Matsuo, A.; Funaki, I.; Nakata, D.; Uchiumi, M.; Higashino, K. Propulsive Performance and Heating Environment of Rotating Detonation Engine with Various Nozzles. *J. Propuls. Power* **2019**, *35*, 213–223. [CrossRef]
16. Oberkampf, W.L.; Trucano, T.G. Verification and Validation in Computational Fluid Dynamics. *Prog. Aerosp. Sci.* **2002**, *38*, 209–272. [CrossRef]
17. Chapman, D.R.; Mark, H.; Pirtle, M.W. Computers vs. Wind Tunnels for Aerodynamic Flow Simulations. *Astronaut. Aeronaut.* **1975**, *13*, 12–35.
18. Smith, B.L. The difference between traditional experiments and CFD validation benchmark experiments. *Nucl. Eng. Des.* **2017**, *312*, 42–47. [CrossRef]
19. Ma, F.; Choi, J.Y.; Yang, V. Thrust Chamber Dynamics and Propulsive Performance of Single-Tube Pulse Detonation Engines. *J. Propuls. Power* **2005**, *21*, 512–526. [CrossRef]
20. Oran, E.S.; Weber, J.W., Jr.; Stefaniw, E.I.; Lefebvre, M.H.; Anderson, J.D., Jr. A Numerical Study of a Two-Dimensional H_2-O_2-Ar Detonation Using a Detailed Chemical Reaction Model. *Combust. Flame* **1998**, *113*, 147–163. [CrossRef]
21. McBride, B.J.; Zehe, M.J.; Gordon, S. *NASA Glenn Coefficients for Calculating Thermodynamics Properties of Individual Species*; NASA-TP-2002-211556; NASA: Washington, DC, USA, 2002.
22. Jachimowski, C.J. *An Analytical Study of the Hydrogen-Air Reaction Mechanism with Application to Scramjet Combustion*; NASA TP-2791; Langley Research Center: Hampton, VA, USA, 1988.
23. Meng, Q.; Zhao, N.; Zheng, H.; Yang, J.; Qi, L. Numerical Investigation of the Effect of Inlet Mass Flow Rates on H2/Air Non-Premixed Rotating Detonation Wave. *Int. J. Hydrogen Energy* **2018**, *43*, 13618–13631. [CrossRef]
24. Sun, J.; Zhou, J.; Liu, S.; Lin, Z.; Cai, J. Effects of Injection Nozzle Exit Width on Rotating Detonation Engine. *Acta Astronaut.* **2017**, *140*, 388–401. [CrossRef]
25. Denisov, Y.N. Structure of Gaseous Detonation in Tubes. *J. Tech. Phys.* **1960**, *30*, 450–459.
26. Kaneshige, M.; Shepherd, J.E. *Detonation Database*; Technical Report FM97-8; California Institute of Technology: Pasadena, CA, USA, 1997.
27. Prakash, S.; Fiévet, R.; Raman, V.; Burr, J.; Yu, K.H. Analysis of the Detonation Wave Structure in a Linearized Rotating Detonation Engine. *AIAA J.* **2020**, *58*, 5063–5077. [CrossRef]
28. Roache, P.J. Quantification of Uncertainty in Computational Fluid Dynamics. *Annu. Rev. Fluid Mech.* **1997**, *29*, 123–160. [CrossRef]
29. Arienti, M. *A Numerical and Analytical Study of Detonation Diffraction*; California Institute of Technology: Pasadena, CA, USA, 2003.
30. Skews, B.W. The Shape of a Diffracting Shock Wave. *J. Fluid Mech.* **1967**, *29*, 297–304. [CrossRef]
31. Guo, C.; Wang, C.; Xu, S.; Zhang, H. Cellular Pattern Evolution in Gaseous Detonation Diffraction in a 90°-Branched Channel. *Combust. Flame* **2007**, *148*, 89–99. [CrossRef]
32. Wang, C.J.; Xu, S.L.; Guo, C.M. Gaseous Detonation Propagation in a Bifurcated Tube. *J. Fluid Mech.* **2008**, *599*, 81–110. [CrossRef]
33. Bedick, C.; Ferguson, D.; Strakey, P. Characterization of Rotating Detonation Engine Injector Response Using Laser-Induced Fluorescence. *J. Propuls. Power* **2019**, *35*, 827–838. [CrossRef]
34. Peraldi, O.; Knystautas, R.; Lee, J.H. Criteria for Transition to Detonation in Tubes. *Symp. (Int.) Combust.* **1988**, *21*, 1629–1637. [CrossRef]
35. Radulescu, M.I.; Mével, R.; Xiao, Q.; Gallier, S. On the Self-Similarity of Diffracting Gaseous Detonations and the Critical Channel Width Problem. *Phys. Fluids* **2021**, *33*, 066106. [CrossRef]
36. Li, H.; Han, W.; Li, J.; Fan, W. Influences of Incoming Flow on Re-Initiation of Cellular Detonations. *Combust. Flame* **2021**, *229*, 111376. [CrossRef]
37. Wang, Y.; Chen, Z.; Chen, H. Diffraction of Weakly Unstable Detonation Through an Obstacle with Different Sizes and Shapes. *Phys. Rev. Fluids* **2021**, *6*, 043201. [CrossRef]
38. Kawasaki, A.; Kasahara, J. A Novel Characteristic Length of Detonation Relevant to Supercritical Diffraction. *Shock Waves* **2020**, *30*, 1–12. [CrossRef]
39. Sun, H.; Kawasaki, A.; Matsuoka, K.; Kasahara, J. A Study on Detonation-Diffraction Reflection Point Distances in H_2/O_2, C_2H_2/O_2, and C_2H_4/O_2 Systems. *Proc. Combust. Inst.* **2021**, *38*, 3605–3613. [CrossRef]

Disclaimer/Publisher's Note: The statements, opinions and data contained in all publications are solely those of the individual author(s) and contributor(s) and not of MDPI and/or the editor(s). MDPI and/or the editor(s) disclaim responsibility for any injury to people or property resulting from any ideas, methods, instructions or products referred to in the content.